ACS OMEGA

Open Access
This article is licensed under CC-BY-NC-ND 4.0

http://pubs.acs.org/journal/acsodf
Article

Formation and Segregation of the Ru- and Rh-MgO Solid Solutions

Kazu Okumura,* Takumi Sasaki, Sou Sugihara, Kotaro Kawaguchi, Anas Abdullahi, and Hikaru Iiyoshi

Cite This: *ACS Omega* 2024, 9, 46129−46137

Read Online

ACCESS | Metrics & More | Article Recommendations | Supporting Information

ABSTRACT: Structural changes in Ru- and Rh-loaded magnesium oxide (MgO) subjected to thermal treatment were investigated by using X-ray absorption spectroscopy. The thermal treatment of the MgO-loaded Ru and Rh nanoparticles led to the formation of Ru-MgO and Rh-MgO solid solutions, respectively. The valences of Ru and Rh in the solutions were 4+ and 3+, respectively, as determined by the Ru and Rh K-edge X-ray absorption near-edge structure (XANES). The degree of solid solution formation was the highest at 873 and 1073 K in Ru-MgO and Rh-MgO, respectively, as observed in the extended X-ray absorption fine structure and XANES analyses. The nearest neighboring Ru−O and Rh−O bond distances were shorter than the Mg−O bond in MgO. The dispersion of Ru and Rh on the MgO surface, measured by CO adsorption, increased for samples thermally heated at 1273 K, suggesting that the segregation of Ru or Rh from the solid solutions occurred at this temperature. Consequently, a relatively high dispersion was realized in the sample thermally heated to 1273 K. A good correlation was found between the dispersion value of Ru in Ru/MgO and the NH_3 decomposition activity.

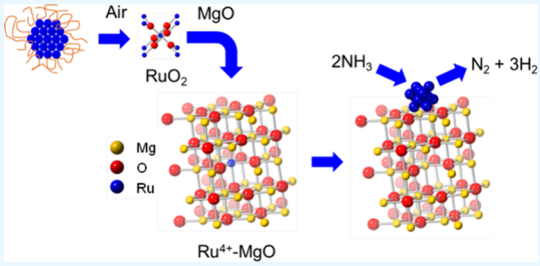

1. INTRODUCTION

Supported rhodium catalysts have been applied as catalysts for purifying exhaust gas from gasoline-powered automobiles and as catalysts for organic syntheses, such as hydrogenation,[1] while supported ruthenium catalysts have been primarily applied in steam reforming of hydrocarbons for obtaining hydrogen.[2] When these catalysts are used in the gas phase, they are used at high temperatures, such as 773 K or higher, which causes a problem of irreversible deterioration due to the agglomeration of metal particles.[3] One of the means for suppressing such irreversible deterioration is by leveraging the metal−support interaction, hindering the agglomeration of active species.[4] This interaction involves the metal species being immobilized on the support through anchoring and forming a solid solution on the support. Such interactions between a metal and support are exemplified by Pt on CeO_2, and Rh or Pd supported on perovskite-based oxides commonly employed for the catalytic conversion of automobile emission gases.[5] These atomically dispersed metal elements have been used in various reactions.[6] By the generation of such a solid solution, it is anticipated that volatile oxides on the support can be retained on the surface. However, in the latter case, the dissolved metal species are inaccessible by the reactants, rendering them ineffective as a catalyst. To activate the metal elements in the solid solution, metal species must be deposited on the surface to be used as catalysts. If the solid−solution metal species can be reprecipitated on the support surface, then well-dispersed and highly active metal species are expected to be obtained. We have previously reported that when metal nanoparticles or complexes of Pd, Ir, and Pt are mixed with MgO and heated, a solid solution is formed, and at approximately 1173 K, the dissolved metal species reprecipitate on the surface of MgO.[7−9] In this study, solid solution formation and subsequent reprecipitation of Ru, Rh, and MgO were investigated primarily through X-ray absorption spectroscopy (XAS) because XAS offers an excellent means of investigating the valency and local structure of various elements. Regarding Ru, while the Ru-MgO solid solution has been partially reported, the detailed formation and reprecipitation processes have not been well clarified. For instance, Prieto reported that metal cations of five kinds of elements (Ru, Rh, Pd, Ir, Pt) are located at the octahedral coordination of MgO in step-edges.[10] Tsang et al. found that on MgO(111), well-dispersed surface Ru ensembles catalyze ammonia decomposition effectively.[11] Also, the efficiency of the ammonia decomposition by Ru/MgO was found to be enhanced by the addition of alkali metal salts.[12] For Rh, although the interactions between Rh with Al_2O_3 and CeO_2 have been reported, there are no reports, to the best of our knowledge, on the solid solution formation between Rh and MgO. If a solid solution can be generated between Ru or Rh and MgO and reprecipitated, it may be possible to regenerate the catalyst deteriorated by sintering. In this study, we investigated the interaction of polyvinylpyrrolidone (PVP) polymer-protected Ru and Rh nanoparticles with MgO. These

Received: July 13, 2024
Revised: October 11, 2024
Accepted: October 17, 2024
Published: November 8, 2024

ACS Publications
© 2024 The Authors. Published by American Chemical Society

https://doi.org/10.1021/acsomega.4c06472
ACS Omega 2024, 9, 46129−46137

PVP polymer-protected nanoparticles have a relatively uniform particle distribution, making them suitable precursors for directly investigating the interaction between metal nanoparticles and MgO. When polymer-protected metal nanoparticles are supported on an oxide surface, they can be kept in a relatively uniform dispersed state.[13] We also investigated samples prepared from the complex of each element at the same time as for the nanoparticles. Furthermore, for Ru-MgO, the decomposition reaction of ammonia was performed and the correlation with the degree of dispersion was investigated, considering that ruthenium catalysts have been extensively researched for storing ammonia as a feedstock and extracting hydrogen to power fuel cells on demand.[14]

2. EXPERIMENTAL SECTION

2.1. Sample Preparation. PVP-stabilized Ru and Rh nanoparticle (Ru, Rh NP) dispersions, diluted with water and ethanol (ethanol:water = 2:8 (vol.)), were impregnated onto MgO. The nanoparticle suspensions of Ru and Rh were obtained from Renaissance Science Co. The diluted NP-dispersed liquid mixed with MgO was evaporated at 313 K, leaving behind a residue that was consequently heated in air with an electric furnace at temperatures ranging from 773 to 1373 K for 3 h in air. MgO (500A) was obtained from Ube Materials Co. Similarly, PVP-stabilized Ru and Rh NPs were loaded onto γ-Al_2O_3 (JRC-ALO-7) and SiO_2 (CARiACT Q-10, Fuji Silisya Co.) using an identical procedure as well. The γ-Al_2O_3 used in this study were sourced from the Catalysis Society of Japan. The initial Ru and Rh loadings were ca. 0.3 wt % each. Unless otherwise noted, Ru and Rh NPs were employed as the precursors for Ru- and Rh-supported MgO, respectively. The samples prepared in this way will henceforth be denoted as Ru or Rh precursor−support. For example, the sample prepared with Ru NPs as a precursor will be denoted as Ru NP-MgO. In the same manner, $(PPh_3)_3RuCl_2$-MgO and $Rh(acac)_3$-MgO were prepared using tris(triphenylphosphine)-ruthenium(II) dichloride ($(PPh_3)_3RuCl_2$) and rhodium(III) acetylacetonate ($Rh(acac)_3$) precursors, respectively. These precursors were sourced from Fujifilm-Wako Pure Chemical Co. These samples were thermally treated in a manner analogous to that of the Ru NP and Rh NP-loaded samples.

2.2. Ru and Rh K-Edge XAS: Data Collection and Analysis. The XAS measurements of the Ru- and Rh-loaded samples were performed on the AR-NW10A beamline using synchrotron radiation, approved by the High Energy Accelerator Research Organization (KEK)'s Photon Factory (KEK-PF-AR), under proposals 2020G621 and 2022G581. Samples were mounted in plastic tubes 6 mm in diameter and about 30 mm long and measured. The data was collected at 298 K, utilizing a Si(311) monochromator in the quick scan mode for 5 min. The double-crystal monochromator was set to full tuning, and no mirrors were used. The beam dimensions were 1.1 mm horizontally and 0.8 mm vertically. Ion chambers filled with argon and krypton gases detected primary and transmitted X-rays, respectively. The extended X-ray absorption fine structure (EXAFS) data were analyzed by first extracting oscillations of $k^3\chi(k)$ data utilizing a spline-smoothing method. For the curve-fitting analysis, to transform the data from k-space, a Fourier transform (FT) was applied to convert the k^3-weighted EXAFS oscillations and $k^3\chi(k)$ data to r-space (typical range: 3−13 $Å^{-1}$). REX software developed by Rigaku Co. was utilized for EXAFS data analysis. EXAFS analysis was performed utilizing a curve-fitting technique with theoretically calculated phase shift and amplitude function using FEFF8 software.[15] The parameters using FEFF were calculated with SIG2 = 0.00360 $Å^2$, S_0^2 = 1.0, and ixc = 0.

2.3. Characterizations of the Samples, Excluding the XAFS Technique. N_2 adsorption/desorption isotherms were obtained using a BELSORP-mini-X instrument (Microtrac Bel Co.) after the samples were evacuated at 573 K. The reduction behavior of the Ru- and Rh-loaded samples was investigated using temperature-programmed reduction (TPR) under a 5% H_2/Ar flow (30 mL min^{-1}) on a BELCAT II instrument (Microtrac Bel Co.) with a temperature ramp rate of 10 K min^{-1}. The effluent gas analysis was conducted using a thermal conductivity detector. Subsequently, after preheating the samples at 923 K in a H_2 flow, the dispersion of Ru and Rh on the supports (MgO, Al_2O_3, and SiO_2) was measured using the BELCAT II instrument, which was used for the TPR measurement. Ru and Rh dispersions were determined using the CO pulse method at 323 K, assuming the CO/metal ratio of 1.0. A JEM-2100 microscope (JEOL Co.) operated at 200 kV was used to obtain transmission electron microscopy (TEM) images. A MiniFlex X-ray diffractometer (Rigaku Co.) was utilized for acquiring X-ray diffraction (XRD) patterns using Cu-Kα radiations.

2.4. Ammonia Decomposition. Ammonia decomposition was performed by using a BELCAT II instrument. A 0.1 g Ru NP-MgO sample mounted in a quartz tube was pretreated under a H_2 flow at 773 K, before being cooled down to 323 K. The sample was then gradually heated to 873 K at a 10 K min^{-1} rate. The reaction used a gas mixture containing 0.5% ammonia in He, which flowed at a rate of 50 mL min^{-1}. The effluent gas was analyzed by using a BELMASS quadrupole mass spectrometer to calculate the N_2 yield. The BELMASS was obtained from Microtrac Bel Co.

2.5. DFT Calculation. Density functional theory (DFT) calculations using the Gaussian program package were carried out to calculate the structure of the Ru-MgO crystal under three-dimensional periodic conditions. The physical wave functions were expanded in terms of accurate numerical basis sets. A double numerical plus d-function was used for all calculations, employing the generalized gradient approximation functional developed by Perdew−Burke−Ernzerhof.[16] Core electrons were treated with effective core potentials. The convergence tolerances for energy, maximum force, and maximum displacement were less than 2.0×10^{-5} Ha, 0.004 Ha/Å, and 0.005 Ha/Å, respectively. A unit cell consists of $Ru_1Mg_{30}O_{32}$, where two nearest Mg atoms were deleted from the perfect crystal of $Mg_{32}O_{32}$ and the deleted two Mg atoms were substituted with a Ru atom to maintain a neutral charge. The cell parameter of the cubic unit cell was 8.42240 Å, which is the same as that for a perfect crystal MgO. Therefore, in the following DFT calculations, the unit cell parameter was the same as that for the original MgO crystal parameters.

3. RESULTS AND DISCUSSION

3.1. Ru and Rh K-Edge EXAFS Investigations. Figure 1a,b presents the EXAFS Fourier transform (EXAFS-FT) of Ru and Rh NP-MgO, -Al_2O_3, and -SiO_2, respectively, after heat treatment in air at 973 K. The corresponding $k^3\chi(k)$ data for Ru- and Rh-loaded samples are displayed in Figure S1a,b, respectively. Accordingly, Tables 1 and 2 list the structural parameters calculated with EXAFS analysis of Ru-MgO and Rh-MgO, and those of MgO, respectively.

https://doi.org/10.1021/acsomega.4c06472
ACS Omega 2024, 9, 46129−46137

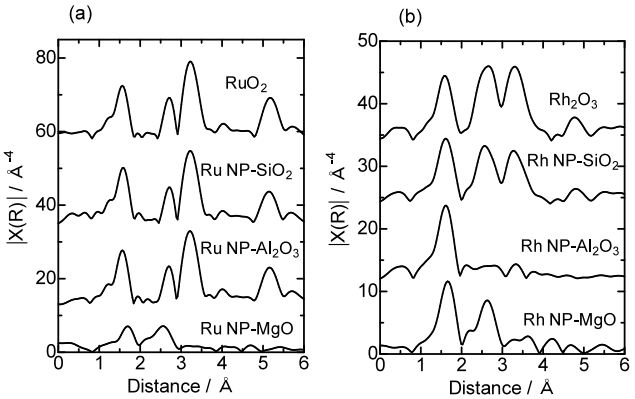

Figure 1. (a) Ru K-edge EXAFS-FT of Ru supported on MgO, Al_2O_3, and SiO_2, heated at 973 K, compared with authentic RuO_2. (b) Rh K-edge EXAFS-FT of Rh supported on MgO, Al_2O_3, and SiO_2, heated at 973 K, compared with that of authentic Rh_2O_3. The FT was performed over the range 3−16 $Å^{-1}$.

The spectra of Ru NP-MgO (Figure 1a) and Rh NP-MgO (Figure 1b) exhibit two peaks at 1.7 and 2.6 Å, differing significantly from those of Ru and Rh NP-Al_2O_3 and -SiO_2, whose spectra closely resemble those of RuO_2 and Rh_2O_3, respectively, except for Rh-Al_2O_3, where the Rh−(O)−Rh bond was not observed probably owing to the formation of well-dispersed Rh species as previously reported.[17] For Ru NP-MgO and Rh NP-MgO, the peak emerging at 1.7 Å was associated with the Ru−O and Rh−O bonds, similar to the bonding pattern of RuO_2 and Rh_2O_3, respectively. The second peak, situated at 2.6 Å, was assignable to the closest-neighboring Ru−Mg and Rh−Mg bonds, as determined by the curve-fitting presented in Table 1. The Ru−Mg and Rh−Mg bond distances were 3.01 and 3.02 Å, respectively, closely matching the closest-neighboring Mg−Mg bond in MgO's salt rock structure, whose bond distance is also 3.01 Å (Table 2). Spinel ($MgRh_2O_4$) formation in Rh-MgO could be ruled out for two reasons. First, the Rh−Mg bond distance found in Rh-MgO was shorter than that of the closest-neighboring Rh−Mg bond (3.40 Å) in $MgRh_2O_4$.[18] Second, EXAFS oscillations and FT of $MgRh_2O_4$ were simulated by FEFF and compared with those of Rh NP-MgO treated at 973 K (Figure S2). EXAFS $k^3\chi(k)$ of $MgRh_2O_4$ shows an increase in the vibration envelope up to k = 15 ($Å^{-1}$) compared to Rh NP-MgO (Figure S2a). EXAFS-FT of $MgRh_2O_4$ shows an enhanced peak intensity in EXAFS-FT compared with that of Rh NP-MgO (Figure S2b). The marked difference between EXAFS vibrations and FT confirms that the $MgRh_2O_4$ spinel was not included in Rh NP-MgO. Then, EXAFS simulated by FEFF based on the model optimized by DFT for Ru-MgO is shown in Figure S3. The structure obtained with DFT calculations for Ru-MgO is shown in Figure S4. The oscillation of EXAFS was similar between the experimentally obtained and simulated EXAFS (Figure S3a). The FT spectra were similar up to the second coordination sphere at 3.0 Å, but the intensity in the third coordination sphere at 3.2 Å was smaller than that in the simulation (Figure S3b). This is probably due to the large amount of Ru present close to the surface of the MgO. The nearest neighboring coordination numbers (CNs) of the Ru−Mg and Rh−Mg bonds were 6.4 ± 1.4 and 7.2 ± 1.0, respectively. These values are significantly lower than those of Mg−Mg with a CN of 12 (Table 2). This is likely because the Ru and Rh ions primarily reside near the surface of MgO in the solid solutions.

Table 2. Structural Data for Nearest Neighboring Mg−O and Mg−Mg of MgO[a]

compound	central atom	neighboring atom	coordination number	distance/Å
MgO	Mg	O	6	2.11
		Mg	12	3.01

[a]Data of X-ray crystallography.

Figure 2a displays the EXAFS-FT analyses of the as-prepared Ru-MgO and those subjected to temperatures ranging from 773 to 1373 K. The corresponding $k^3\chi(k)$ values are presented in Figure S5a. The EXAFS-FT spectrum of the as-prepared sample features a peak at 1.6 Å attributed to the Ru−O bond, indicating that the loaded Ru NP underwent oxidation during sample preparation. Upon heating at 773 K, a new peak emerged at 2.6 Å, corresponding to the Ru−Mg bonds, confirming the creation of a Ru-MgO solid solution. Further

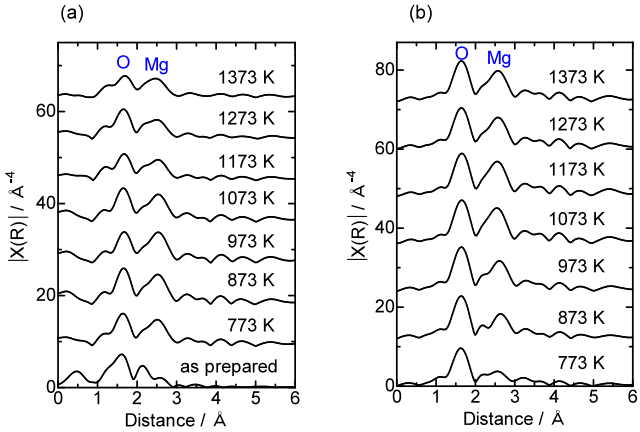

Figure 2. (a) Ru K-edge EXAFS-FT of Ru NP-MgO, and (b) Rh K-edge EXAFS-FT of Rh NP-MgO heated at various temperatures. The FT was conducted over the range 3−13 $Å^{-1}$.

Table 1. Curve-Fitting Parameters Derived from Ru and Rh K-Edge EXAFS Data, Collected at 298 K, for Ru NP-MgO and Rh NP-MgO Samples Heated at 973 K[a]

central atom	scatterer	coordination number	distance/Å	ΔE_0/eV[b]	Debye−Waller factor/Å	residual factor/%
Ru	O	6.3 ± 1.6	2.06 ± 0.02	0 ± 4	0.094 ± 0.026	1.0
	Mg	6.4 ± 1.4	3.01 ± 0.01	−5 ± 2	0.066 ± 0.026	
Rh	O	6.6 ± 0.6	2.06 ± 0.01	−1 ± 3	0.059 ± 0.027	1.2
	Mg	7.2 ± 1.0	3.02 ± 0.01	−4 ± 2	0.068 ± 0.031	

[a]FT and filtering range were 30−130 nm^{-1} and 1.3−3.5 Å. [b]Correction applied to account for the energy difference of the photoelectron between the sample and the reference.

https://doi.org/10.1021/acsomega.4c06472
ACS Omega 2024, 9, 46129−46137

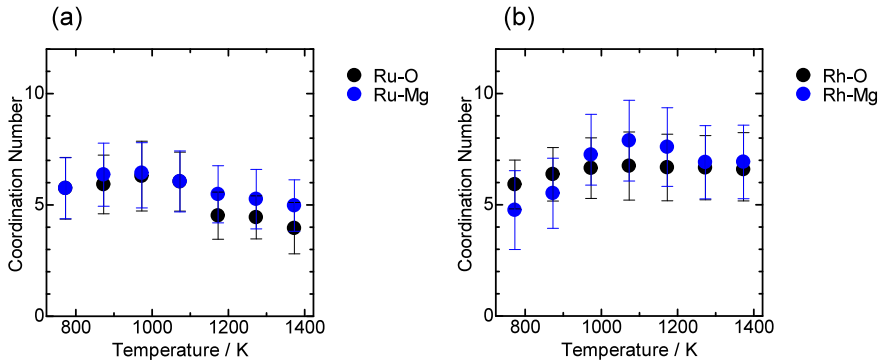

Figure 3. Nearest neighboring bond CNs against treatment temperature for (a) Ru−O and Ru−Mg bonds in Ru NP-MgO determined by Ru K-edge EXAFS and (b) Rh−O and Rh−Mg bonds in Rh NP-MgO determined by Rh K-edge EXAFS.

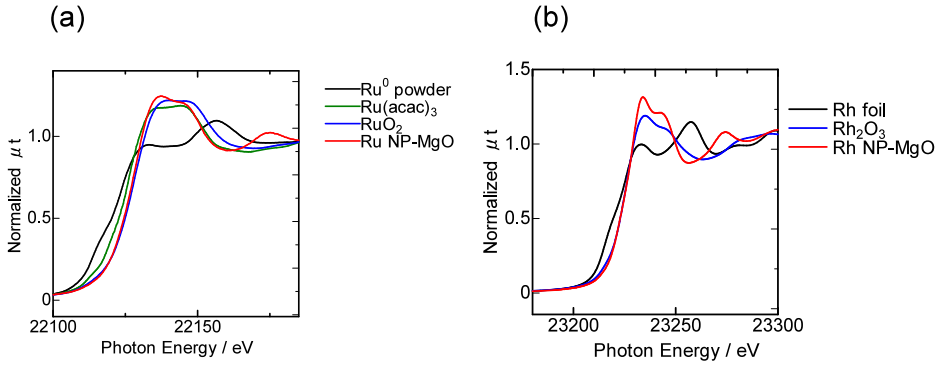

Figure 4. (a) Ru K-edge XANES profiles of Ru NP-MgO heated at 1073 K and reference samples (Ru^0 powder, $Ru(acac)_3$, and RuO_2). (b) Rh K-edge XANES profiles of Rh NP-MgO heated at 1073 K and reference samples (Rh foil, Rh_2O_3).

heating to 973 K resulted in the growth of the Ru−O bond, while a subsequent temperature increase to 1373 K weakened the Ru−Mg peak bond. A similar change was observed for $(PPh_3)_3RuCl_2$-MgO prepared using $(PPh_3)_3RuCl_2$ as the precursor (Figure S6a,b).

Figure 3a depicts the variation of CNs of the Ru−O and Ru−Mg bonds in Ru-MgO with temperature. The corresponding curve fittings for 773, 973, and 1373 K are displayed in Figure S7. Ru−O and Ru−Mg bonds emerged in the samples heated at 773 K, with the CN of the bond Ru−Mg increasing up to 973 K and then decreasing gradually with further temperature elevation up to 1373 K, suggesting that the Ru−MgO bond likely segregated in this temperature range. Additionally, the Ru−O and Ru−Mg bond distances in Ru−MgO are plotted against temperature in Figure S8a, revealing no change in the distances with temperature. The bond distance of the closest-neighboring Ru−O bond (2.06 Å) was slightly shorter compared with the Mg−O bond distance of 2.11 Å, consistent with findings in Ir-MgO, Pt-MgO, and Pd-MgO solid solutions.[7−9] This phenomenon is likely attributable to the higher valence of Ru^{4+} compared with Mg^{2+}, leading to a stronger attraction to the O^{2-} anion by the Ru^{4+}, and consequently a shorter Ru^{4+}−O^{2-} bond length in the Ru-MgO solid solution.

Figure 2b presents the EXAFSFTs of Rh NP-MgO subjected to temperatures ranging from 773 to 1373 K, with the corresponding $k^3\chi(k)$ data provided in Figure S5b. The corresponding curve fittings for 773, 973, and 1373 K are displayed in Figure S9. Rh-MgO solid solutions proceeded up to 1073 K, as evidenced by the increased CN of the Rh−Mg bond within this temperature range, as depicted in Figure 3b. With further temperature increases, a decrease in the CN of the Rh−Mg bond was observed (Figure 3b), likely because the Rh-MgO solid solution segregated to produce dispersed Rh species and MgO, akin to observations made for Ru-MgO. A similar trend was observed for $Rh(acac)_3$-MgO synthesized using $Rh(acac)_3$ as the precursor (Figure S6c,d). The result of the curve-fitting for Rh-MgO heated at 973 K is included in Table 1. The Rh−O and Rh−Mg bond distances were close to those of Ru−O and Ru−Mg in Ru-MgO, wherein the Rh−O and Rh−Mg bond distances were 2.06 and 3.02 Å, respectively. The distances remained unchanged across varying treatment temperatures, as presented in Figure S8b.

3.2. Ru and Rh K-Edge XANES Studies. Figure 4a,b presents the Ru and Rh K-edge X-ray absorption near-edge structure (XANES) profiles of Ru NP-MgO and Rh NP-MgO heated at 1073 K, along with those of the reference samples, respectively. As discussed above, the confirmation of solid solution formation in the samples heated at 1073 K was achieved by Ru and Rh K-edge EXAFS. Ru K-edge XANES profiles (Figure 4a) exhibit a shift in the inflection points and peak maxima of the white line to higher energies, correlating with the increasing valence of Ru in the reference samples (Ru^0 powder, $Ru(acac)_3$, and RuO_2). Similarly, Rh K-edge XANES of the Rh foil and Rh_2O_3 (Figure 4b) show a comparable shift in the inflection points and peak maxima, consistent with previous reports.[19] In these cases, the Ru and Rh K-edge white lines originate from the transition from the 1s state to the unoccupied 5p state. The inflection point energies in the XANES profiles of Ru NP-MgO and Rh NP-MgO match those of RuO_2 (22,124 eV) and Rh_2O_3 (23,229 eV), respectively, indicating that the valences of Ru and Rh in the solid solutions

https://doi.org/10.1021/acsomega.4c06472
ACS Omega 2024, 9, 46129−46137

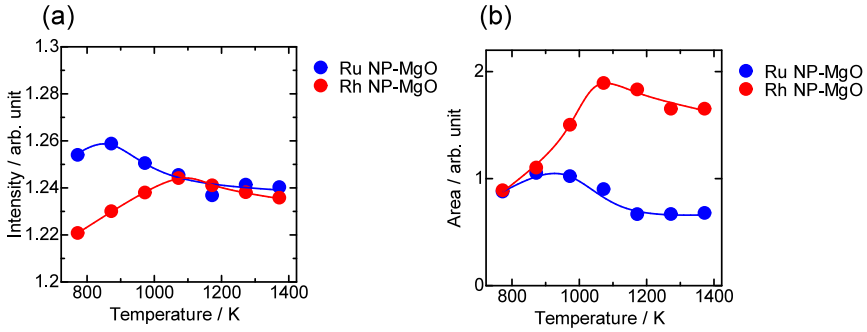

Figure 5. (a) Intensity of the white lines at 22,138 and 23,238 eV in the Ru-K, Rh-K edge XANES of Ru NP-MgO and Rh NP-MgO, respectively, plotted against treatment temperature. (b) Area of the peaks appeared at 22,175 and 23,248 eV in the Ru-K, Rh-K edge XANES of Ru NP-MgO and Rh NP-MgO, respectively, plotted against treatment temperature.

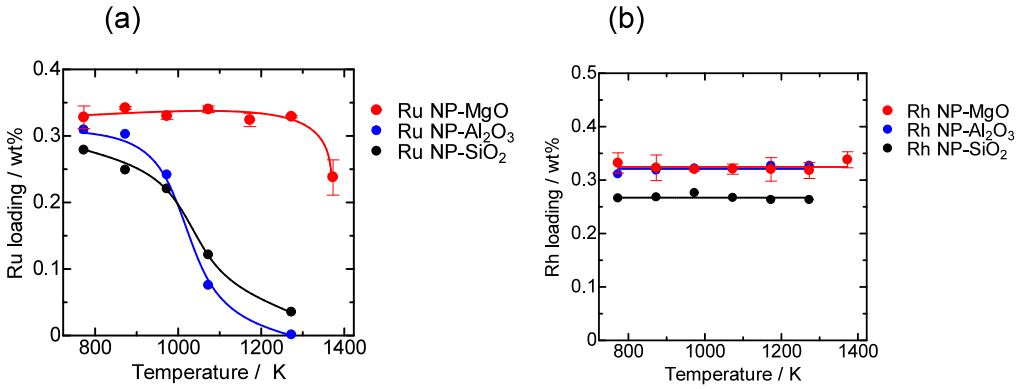

Figure 6. Dependence of (a) Ru loadings and (b) Rh loadings on the treatment temperature of MgO-, Al_2O_3-, and SiO_2-loaded samples.

are 4+ and 3+, respectively. However, the intensities of the white lines observed for Ru NP-MgO (22,137 eV) and Rh NP-MgO (23,234 eV) were larger than those of RuO_2 and Rh_2O_3, respectively. Generally, the white line intensity of the K-edge XANES is correlated to the density of the unoccupied orbitals. Nevertheless, the intensity and shape of the K-edge XANES spectra exhibit variations depending on the extent of the ionic and covalent characters of Ru and Rh.[20] Likely, the strong ionic character of Ru and Rh cations and the octahedral symmetry around them caused the enhanced intensity of this white line. Similar enhancements of the white line in comparison with the corresponding oxides were found in the Ir L_3-edge of Ir-MgO,[8] the Pt L_3-edge of Pt-MgO,[9] and the Pd K-edges of Pd-MgO solid solutions.[7]

Figure 5a displays the plot of the white line intensities against the treatment temperature, with the maximum intensities observed for Ru-MgO and Rh-MgO heated at 873 and 1073 K, respectively, suggesting that solid solution formation proceeded most at these temperatures. Additionally, characteristic peaks appeared in the Ru- and Rh-edge XANES profiles at 22,175 and 23,274 eV for Ru NP-MgO and Rh NP-MgO, respectively (Figure 4a,b), similar to those found in the L_3-edge XANES of Ir-MgO,[8] Pt-MgO,[9] and Pd K-edge XANES of the Pd-MgO solid solutions[7] but absent in the reference samples. This difference suggests that the peaks originated from the photoelectrons interfered with by Mg^{2+} ions closest to the Ru^{4+} and Rh^{3+} ions. In fact, this peak was also reproduced by XANES calculated by FEFF on the basis of the Ru-MgO structure optimized by DFT calculations (Figure S10). The area of the peak is depicted against the treatment temperature in Figure 5b. An example of the area calculation for Ru NP-MgO is shown in Figure S11. This trend was similar to that of the white line intensity (Figure 5a), in that the highest values were observed at 873 and 1073 K for Ru NP-MgO and Rh NP-MgO, respectively. For Ru NP-MgO and Rh NP-MgO, the area of this peak decreases above 873 and 1073 K, respectively, suggesting that segregation occurred gradually with increasing treatment temperature up to 1373 K.

3.3. Ru and Rh Loading. In Figure 6a, Ru loadings of Ru NP-Al_2O_3, -SiO_2, and -MgO are plotted against the treatment temperature. The loading was determined by analyzing the edge jump of the K-edge XANES spectrum and the sample mass, calibrated by reference samples. The Ru loading in Ru NP-Al_2O_3 and Ru NP-SiO_2 significantly decreased as the temperature rose from 773 to 1273 K. The marked decrease in Ru loading in Ru NP-Al_2O_3 and Ru NP-SiO_2 was caused by the removal of the formed volatile RuO_2 on the surfaces of Al_2O_3 and SiO_2.[21] By contrast, Ru loading in Ru NP-MgO remained unchanged up to 1273 K due to stable Ru-MgO solid solution formation. For the Rh-loaded samples, the loading did not change upon heating to 1273 or 1373 K (Figure 6b). This is due to the nonvolatile nature of Rh oxide, in contrast to Ru oxide.[22]

3.4. TEM Studies. Figure 7a,b shows the TEM images of the as-prepared and heated Ru NP-MgO samples at 1073 K, respectively. Ru NPs were not observed in the as-prepared sample, even though the Ru nanoparticles were supported during preparation. The structure of the nanoparticles likely collapsed because of the oxidation of Ru in the loading stage, as observed in the Ru EXAFS spectrum in Figure 2a. The facile oxidation of metal Ru agreed with the observation of scanning tunneling microscopy.[23] NPs were not observed in the 1073 K-

https://doi.org/10.1021/acsomega.4c06472
ACS Omega 2024, 9, 46129−46137

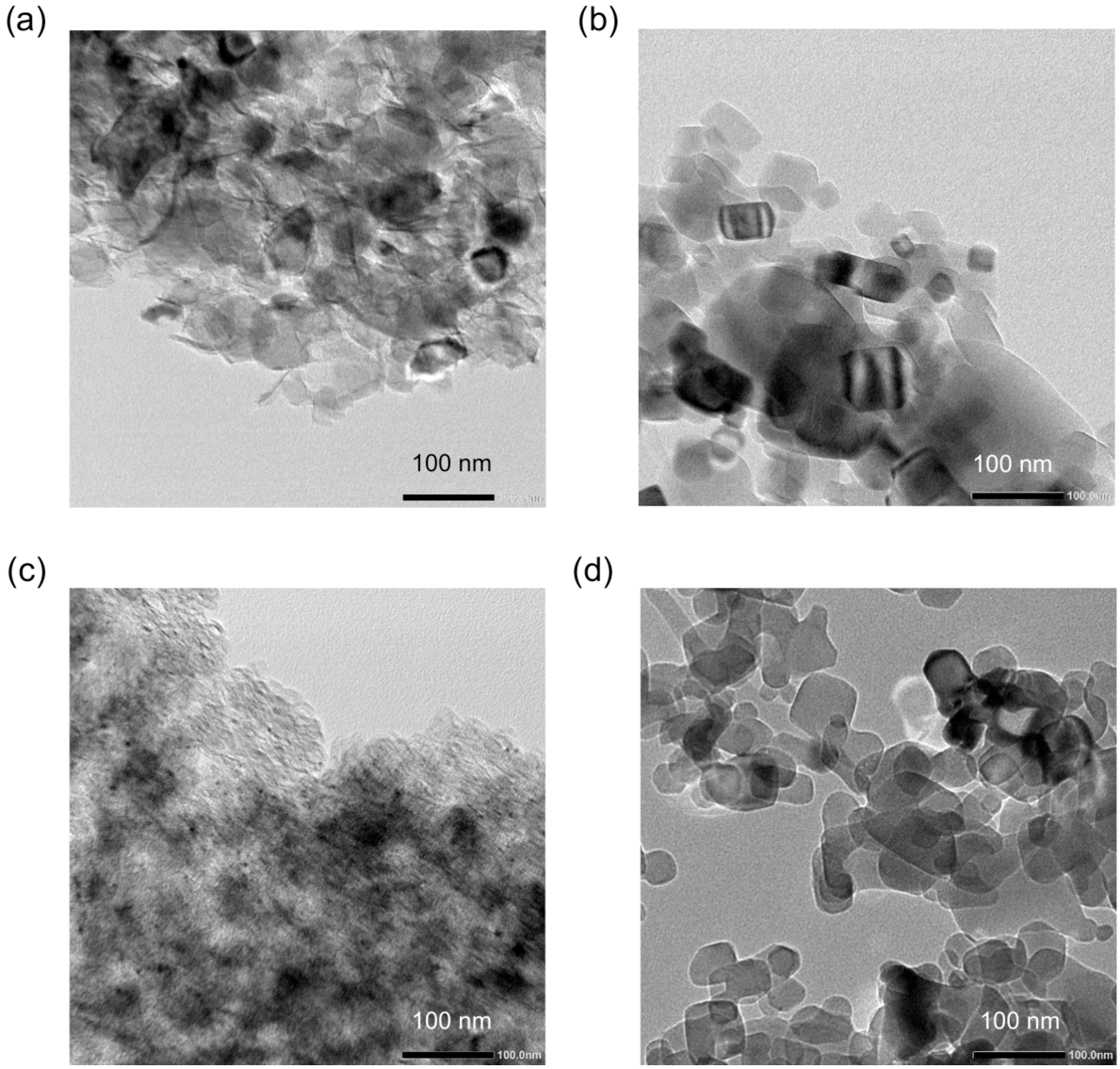

Figure 7. TEM images of Ru NP-MgO: (a) as-prepared sample and (b) the sample after heating at 1073 K. TEM images of Rh NP-MgO: (c) as-prepared sample and (d) the sample after heating at 1073 K.

treated samples, in which aggregated MgO crystals were observed (Figure 7b). Regarding Rh NP-MgO, the TEM image of the as-prepared Rh NP-MgO shows Rh particles approximately 1−4 nm in diameter well-dispersed on the support (Figure 7c). Rh NPs were no longer observed in the 1073 K-treated samples (Figure 7d). Instead, angular MgO particles were observed, likely resulting from the sintering of MgO and the concomitant Rh-MgO solid solution formation.

3.5. XRD Patterns and Nitrogen Adsorption Isotherms. Figure S12a−c shows the XRD patterns of Ru NP-MgO, Rh NP-MgO, and MgO heated at various temperatures, respectively. The XRD patterns of Ru NP-MgO and Rh NP-MgO matched that of MgO, and no additional peaks corresponding to RuO_2 or Rh_2O_3 were observed.[24] Figure 8 shows the plot of the MgO(200) facet diffraction intensity emerging at 42.8° for Ru NP-MgO, Rh NP-MgO, and unloaded MgO against the treatment temperature. At the same treatment temperature, the MgO(200) diffraction intensity in Ru- and Rh NP-MgO was higher than that of unloaded MgO, likely because the Mg^{2+} ions in MgO were replaced with Ru^{4+} and Rh^{3+} ions, resulting in an enhanced

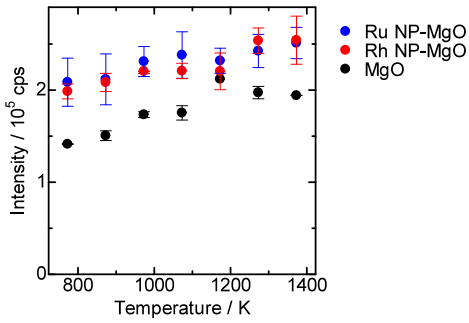

Figure 8. Intensity of MgO(200) diffraction in the XRD patterns of Ru NP-MgO, Rh NP-MgO, and unloaded MgO plotted against the treatment temperature.

MgO lattice. This enhancement was selective to the MgO(200) facet, consistent with observations in Ir- and Pt-MgO solid solutions.[8,9]

The N_2 adsorption isotherms of Ru NP-MgO, Rh NP-MgO, and MgO are displayed in Figure S13. The Brunauer−

https://doi.org/10.1021/acsomega.4c06472
ACS Omega 2024, 9, 46129−46137

Emmett–Teller (BET) method was applied to calculate the specific surface area, and the values are presented in Figure S14. The higher BET surface area of the 573 K-heated samples compared to MgO was probably attributed to the partial $Mg(OH)_2$ formation during Ru and Rh NP loading on the MgO surface.[25] The specific surface areas of Ru NP-MgO and Rh NP-MgO were approximately 20 m^2 g^{-1}, and the values remained unchanged with the treatment temperature between 673 and 1373 K, indicating a negligible surface area decrease due to thermal sintering.

3.6. H_2-TPR Profiles. Figure 9a shows the H_2-TPR plots of Ru NP-MgO heated at various temperatures. The H_2 consumption was negligible for the samples heated at 773–1073 K, evident from the flat TPR peaks. In contrast, significant H_2 consumption was observed at 690 K for the sample heated at 1273 K, attributed to the reduction of Ru^{4+} to Ru^0.[26] No hydrogen consumption peak was apparent below 1073 K, indicating Ru formed a nonreducible solid solution with MgO; hence, H_2 was not consumed. By contrast, Ru^{4+} segregated at 1273 K on the surface of MgO and was consequently reduced with H_2 during the H_2-TPR measurements. In the H_2-TPR profiles of Rh NP-MgO heated at 1273 and 1373 K, the H_2 consumption peak emerged at ∼680 K, whereas the peak was not apparent in the samples heated at temperatures lower than 1173 K (Figure 9b).

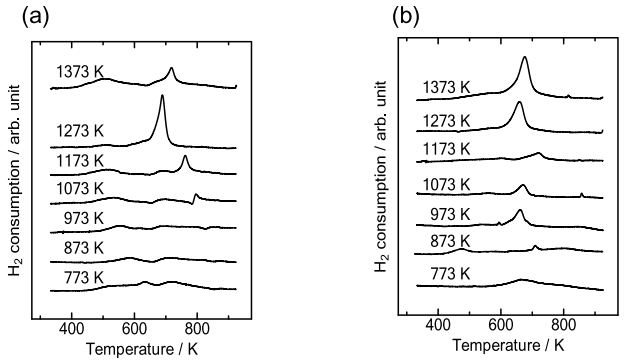

Figure 9. H_2-TPR profiles of (a) Ru NP-MgO and (b) Rh NP-MgO treated at various temperatures. The numbers on the curves indicate the treatment temperatures.

3.7. Dispersion of Ru and Rh Measured by CO Adsorption. Figure 10a displays the dispersion values of Ru loaded on MgO, Al_2O_3, and SiO_2 plotted against the treatment temperature. The dispersion of Ru NP-Al_2O_3 was <5%, whereas that of Ru NP-SiO_2 was negligible. The low dispersion of these samples may be due to the formation of aggregated RuO_2 as observed by Ru K-edge EXAFS (Figure 1a). By contrast, the dispersion values of Ru in Ru-MgO were substantially larger than those in Ru NP-Al_2O_3 and Ru NP-SiO_2; the value tended to increase monotonically with an increase in the treatment temperature, except for that treated at 973 K. The highest dispersion (32%) was achieved for the sample treated at 1373 K. For the Rh-loaded samples, the dispersions of Rh NP-Al_2O_3 and Rh NP-SiO_2 decreased with an increasing treatment temperature (Figure 10b). The relatively high dispersion (67%) of Rh NP-Al_2O_3 treated at 773 K was consistent with the literature.[27] The behavior of Rh-MgO was significantly different from that of Rh NP-Al_2O_3 and Rh NP-SiO_2, in which a U-shape was observed, with the highest dispersion value of 41% obtained at 1273 K. The surface migration of Ru and Rh on MgO likely led to their reduction with H_2, facilitating CO adsorption on metallic Ru and Rh in samples heated at 1173 and 1273 K. The migration of Ru and Rh with increasing temperature was supported by Ru and Rh K-edge EXAFS, where a decrease in the CNs of Ru–Mg and Rh–Mg bonds was observed at the corresponding temperatures (Figure 3a,b). A comparable change in dispersion was observed for Ir and Pt loaded onto MgO,[8,9] suggesting that the segregation of these elements commonly occurred on MgO. In agreement with the dispersion change, a large consumption peak of H_2 was observed in the H_2-TPR profiles of Ru NP-MgO and Rh NP-MgO at approximately 1273 K, implying that the segregation of Ru and Rh in these solid solutions occurred (Figure 9).

3.8. Ammonia Decomposition over Ru NP-MgO. Ammonia decomposition was performed over Ru NP-MgO that was thermally treated at various temperatures. The samples underwent reduction under a H_2 stream at 773 K before the reaction based on the reported method.[28] Figure 11a shows the yield of N_2 plotted against the treatment temperature. The onset temperature of NH_3 decomposition was dependent on the heat treatment temperature, with the sample heated to 1273 K having the lowest onset temperature. The highest activity was observed for the sample heated at 1273 K as presented in Figure 11b, in which the conversion corresponding to a 50% N_2 yield was obtained. At this temperature, a relatively high Ru dispersion of 27% was achieved. Therefore, the high activity of the sample at 1273 K may be due to the relatively high degree of dispersion of Ru

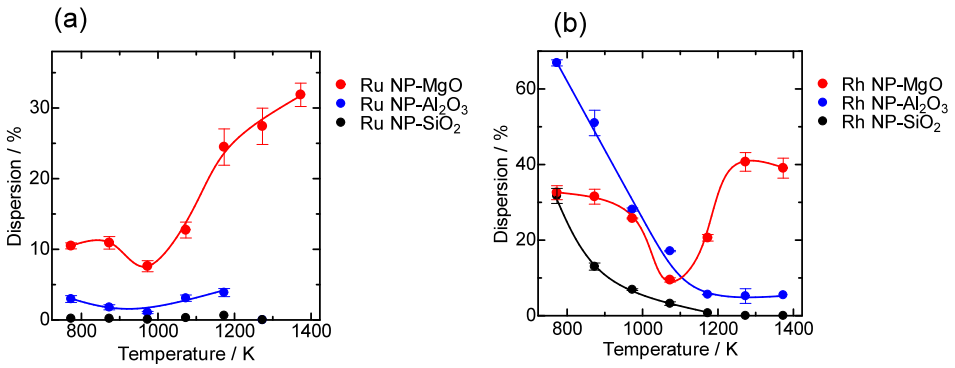

Figure 10. Dependence of (a) Ru dispersion in Ru NP-MgO, Ru NP-Al_2O_3, and Ru NP-SiO_2 and (b) Rh dispersion in Rh NP-MgO, Rh NP-Al_2O_3, and Rh NP-SiO_2 on the treatment temperature.

https://doi.org/10.1021/acsomega.4c06472
ACS Omega 2024, 9, 46129–46137

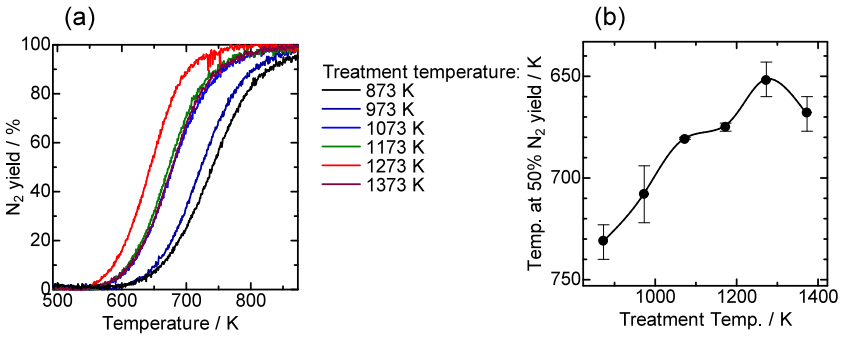

Figure 11. (a) Temperature dependence of the yield of N_2 in NH_3 decomposition over Ru NP-MgO treated at various temperatures. (b) Temperature at which 50% conversion of NH_3 was attained over Ru NP-MgO against the treatment temperature.

deposited on the MgO surface. The exceptionally low activity of the sample treated at 1373 K may be due to the lower Ru loading, as shown in Figure 6a, which may have been caused by the partial sublimation of RuO_2. In addition to this, a good correlation was observed between the N_2 yield in NH_3 decomposition and the H_2-TPR values shown in Figure 9a. The samples heat-treated at 1173−1373 K are highly active in ammonia decomposition, and these samples show a clear hydrogen consumption peak in the H_2-TPR. In particular, the sample heat-treated at 1273 K exhibits the highest activity, but this sample shows the largest hydrogen consumption peak. These results suggest that the Ru particles redeposited by heat treatment of the Ru-MgO solid solution with MgO above 1173 K are highly active in the decomposition of ammonia. While most conventional catalysts are prepared by supporting Ru species on a substrate, this study proposes a new method of preparing highly dispersed Ru catalysts by a bottom-up method in which Ru is precipitated after forming a solid solution.

4. CONCLUSIONS

The formation and segregation of Ru and Rh loaded onto MgO were monitored using XAFS. Formation of the Ru-MgO and Rh-MgO solid solution was found after treatment of Ru- and Rh-supported MgO at around 873−1073 K. Through comparison of the XANES spectra of the reference samples, the valences of Ru and Rh in Ru-MgO and Rh-MgO solid solutions were determined to be 4+ and 3+, respectively. The Ru and Rh species formed solid solutions segregated at temperatures exceeding 1173 K on the surface of MgO. The segregated samples exhibited high dispersion, as measured by CO adsorption. The behavior observed with Ru- and Rh-loaded MgO was significantly different from those loaded on Al_2O_3 and SiO_2, in which the dispersion was negligible or decreased markedly with an increase in the treatment temperature, probably owing to the progress of sintering. Furthermore, we found that the treatment temperature of Ru-MgO influenced the ammonia decomposition activity. The formation and segregation of a solid solution with MgO are effective methods to maintain a high dispersion of metal species at a temperature of ∼1173 K.

■ ASSOCIATED CONTENT

Supporting Information

The Supporting Information is available free of charge at https://pubs.acs.org/doi/10.1021/acsomega.4c06472.

EXAFS and XANES; XRD patterns; N_2 adsorption isotherms and specific surface area; and DFT optimized crystal structure and bond distances (PDF)

■ AUTHOR INFORMATION

Corresponding Author

Kazu Okumura − *Department of Applied Chemistry, School of Advanced Engineering, Kogakuin University, 192-0015 Tokyo, Japan*; orcid.org/0000-0002-7952-3482; Email: okmr@cc.kogakuin.ac.jp

Authors

Takumi Sasaki − *Department of Applied Chemistry, School of Advanced Engineering, Kogakuin University, 192-0015 Tokyo, Japan*

Sou Sugihara − *Department of Applied Chemistry, School of Advanced Engineering, Kogakuin University, 192-0015 Tokyo, Japan*

Kotaro Kawaguchi − *Department of Applied Chemistry, School of Advanced Engineering, Kogakuin University, 192-0015 Tokyo, Japan*

Anas Abdullahi − *Department of Applied Chemistry, School of Advanced Engineering, Kogakuin University, 192-0015 Tokyo, Japan*

Hikaru Iiyoshi − *Department of Applied Chemistry, School of Advanced Engineering, Kogakuin University, 192-0015 Tokyo, Japan*

Complete contact information is available at: https://pubs.acs.org/10.1021/acsomega.4c06472

Notes

The authors declare no competing financial interest.

■ ACKNOWLEDGMENTS

This research was supported by the Ministry of Education, Science, Sports and Culture, Grant-in-Aid for Scientific Research (C), 22K04833, 2022-2024.

■ REFERENCES

(1) Roy, S.; Hegde, M.; Madras, G. Catalysis for NOx abatement. *Appl. Energy* **2009**, *86* (11), 2283−2297. Fagnou, K.; Lautens, M. Rhodium-catalyzed carbon−carbon bond forming reactions of organometallic compounds. *Chem. Rev.* **2003**, *103* (1), 169−196.

(2) Clarke, S. H.; Dicks, A. L.; Pointon, K.; Smith, T. A.; Swann, A. Catalytic aspects of the steam reforming of hydrocarbons in internal reforming fuel cells. *Catal. Today* **1997**, *38* (4), 411−423.

(3) Zhang, Z.; Tsipouriari, V. A.; Efstathiou, A. M.; Verykios, X. E. Reforming of methane with carbon dioxide to synthesis gas over

supported rhodium catalysts: I. Effects of support and metal crystallite size on reaction activity and deactivation characteristics. *J. Catal.* **1996**, *158* (1), 51−63.

(4) Shinjoh, H. Noble metal sintering suppression technology in three-way catalyst: automotive three-way catalysts with the noble metal sintering suppression technology based on the support anchoring effect. *Catal. Surv. Asia* **2009**, *13* (3), 184−190.

(5) Hatanaka, M.; Takahashi, N.; Tanabe, T.; Nagai, Y.; Dohmae, K.; Aoki, Y.; Yoshida, T.; Shinjoh, H. Ideal Pt loading for a Pt/CeO_2-based catalyst stabilized by a Pt−O−Ce bond. *Appl. Catal. B* **2010**, *99* (1−2), 336−342. Tanaka, H.; Uenishi, M.; Taniguchi, M.; Tan, I.; Narita, K.; Kimura, M.; Kaneko, K.; Nishihata, Y.; Mizuki, J. The intelligent catalyst having the self-regenerative function of Pd, Rh and Pt for automotive emissions control. *Catal. Today* **2006**, *117* (1−3), 321−328.

(6) Zhang, Z.; Li, H.; Wu, D.; Zhang, L.; Li, J.; Xu, J.; Lin, S.; Datye, A. K.; Xiong, H. Coordination structure at work: Atomically dispersed heterogeneous catalysts. *Coord. Chem. Rev.* **2022**, *460*, No. 214469.

(7) Okumura, K.; Morita, S.; Iiyoshi, H.; Takaba, H. Formation and Segregation of a Pd−MgO Solid Solution Studied by X-ray Absorption Spectroscopy. *ACS omega* **2023**, *8* (8), 7507−7516.

(8) Okumura, K.; Hoshi, H.; Iiyoshi, H. Formation of Ir−MgO Solid Solutions Analyzed with X-ray Absorption Spectroscopy. *Catal. Surv. Asia* **2023**, *27* (1), 95−106.

(9) Okumura, K.; Hoshi, H.; Iiyoshi, H.; Takaba, H. Formation of a Pt−MgO solid solution: analysis by X-ray absorption fine structure spectroscopy. *ACS omega* **2022**, *7* (31), 27458−27468.

(10) Sarma, B. B.; Plessow, P. N.; Agostini, G.; Concepción, P.; Pfänder, N.; Kang, L.; Wang, F. R.; Studt, F.; Prieto, G. Metal-specific reactivity in single-atom catalysts: CO oxidation on 4d and 5d transition metals atomically dispersed on MgO. *J. Am. Chem. Soc.* **2020**, *142* (35), 14890−14902.

(11) Fang, H.; Wu, S.; Ayvali, T.; Zheng, J.; Fellowes, J.; Ho, P.-L.; Leung, K. C.; Large, A.; Held, G.; Kato, R.; Suenaga, K.; Reyes, Y. I. A.; Thang, H. V.; Chen, H.-Y. T.; Tsang, S. C. E. Dispersed surface Ru ensembles on MgO(111) for catalytic ammonia decomposition. *Nat. Commun.* **2023**, *14* (1), 647.

(12) Zhang, J.; Xu, H.; Ge, Q.; Li, W. Highly efficient Ru/MgO catalysts for NH_3 decomposition: Synthesis, characterization and promoter effect. *Catal. Commun.* **2006**, *7* (3), 148−152.

(13) Song, H.; Rioux, R. M.; Hoefelmeyer, J. D.; Komor, R.; Niesz, K.; Grass, M.; Yang, P.; Somorjai, G. A. Hydrothermal growth of mesoporous SBA-15 silica in the presence of PVP-stabilized Pt nanoparticles: synthesis, characterization, and catalytic properties. *J. Am. Chem. Soc.* **2006**, *128* (9), 3027−3037.

(14) Liu, H. *Ammonia synthesis catalysts: innovation and practice*; World Scientific, 2013. Schüth, F.; Palkovits, R.; Schlögl, R.; Su, D. S. Ammonia as a possible element in an energy infrastructure: catalysts for ammonia decomposition. *Energy Environ. Sci.* **2012**, *5* (4), 6278−6289.

(15) Ankudinov, A. L.; Ravel, B.; Rehr, J.; Conradson, S. Real-space multiple-scattering calculation and interpretation of x-ray-absorption near-edge structure. *Phys. Rev. B* **1998**, *58* (12), 7565.

(16) Perdew, J. P.; Burke, K.; Ernzerhof, M. Generalized gradient approximation made simple. *Phys. Rev. Lett.* **1996**, *77* (18), 3865.

(17) Asakura, H.; Hosokawa, S.; Ina, T.; Kato, K.; Nitta, K.; Uera, K.; Uruga, T.; Miura, H.; Shishido, T.; Ohyama, J.; Satsuma, A.; Sato, K.; Yamamoto, A.; Hinokuma, S.; Yoshida, H.; Machida, M.; Yamazoe, S.; Tsukuda, T.; Teramura, K.; Tanaka, T. Dynamic behavior of Rh species in Rh/Al_2O_3 model catalyst during three-way catalytic reaction: an operando X-ray absorption spectroscopy study. *J. Am. Chem. Soc.* **2018**, *140* (1), 176−184. Machida, M.; Uchida, Y.; Ishikawa, Y.; Hinokuma, S.; Yoshida, H.; Ohyama, J.; Nagao, Y.; Endo, Y.; Iwashina, K.; Nakahara, Y. Thermostable Rh metal nanoparticles formed on Al_2O_3 by high-temperature H_2 reduction and its impact on three-way catalysis. *J. Phys. Chem. C* **2019**, *123* (40), 24584−24591.

(18) Jacob, K.; Prusty, D.; Kale, G. Phase relations and Gibbs energies of spinel phases and solid solutions in the system Mg−Rh−O. *J. Alloys Compd.* **2012**, *513*, 365−372.

(19) Altwasser, S.; Gläser, R.; Lo, A. S.; Liu, P.-H.; Chao, K.-J.; Weitkamp, J. Incorporation of RuO_2 nanoparticles into MFI-type zeolites. *Microporous Mesoporous Mater.* **2006**, *89* (1−3), 109−122. Gao, P.; Liang, G.; Ru, T.; Liu, X.; Qi, H.; Wang, A.; Chen, F.-E. Phosphorus coordinated Rh single-atom sites on nanodiamond as highly regioselective catalyst for hydroformylation of olefins. *Nat. Commun.* **2021**, *12* (1), 4698.

(20) Yang, C.; Wu, Z.; Zhao, Z.; Gao, Y.; Ma, T.; Luo, X.; Cheng, C.; Wang, Y.; Li, S.; Zhao, C. Mn-Oxygen Compounds Coordinated Ruthenium Sites with Deprotonated and Low Oxophilic Micro-environments for Membrane Electrolyzer-based H_2-Production. *Adv. Mater.* **2023**, *35*, No. 2303331. Kroner, A. B.; Newton, M. A.; Tromp, M.; Russell, A. E.; Dent, A. J.; Evans, J. Structural Characterization of Alumina-Supported Rh Catalysts: Effects of Ceriation and Zirconiation by using Metal−Organic Precursors. *ChemPhysChem* **2013**, *14* (15), 3606−3617.

(21) Ji, L.; Lin, J.; Zeng, H. Thermal processes of volatile RuO_2 in nanocrystalline Al_2O_3 matrixes involving $\vec{\gamma}$ α phase transformation. *Chem. Mater.* **2001**, *13* (7), 2403−2412.

(22) Inabinett, D.; Knight, T.; Adams, T.; Gray, J. Study of XeF_2 fluorination potential against Rh_2O_3, RuO_2, ZrO_2, and U_3O_8 for use in reactive gas recycle of used nuclear fuel. *Prog. Nucl. Energy* **2014**, *76*, 106−111.

(23) Herd, B.; Goritzka, J. C.; Over, H. Room temperature oxidation of ruthenium. *J. Phys. Chem. C* **2013**, *117* (29), 15148−15154.

(24) Larimi, A. S.; Kazemeini, M.; Khorasheh, F. Highly selective doped PtMgO nano-sheets for renewable hydrogen production from APR of glycerol. *Int. J. Hydrogen Energy* **2016**, *41* (39), 17390−17398.

(25) Hanlon, J. M.; Diaz, L. B.; Balducci, G.; Stobbs, B. A.; Bielewski, M.; Chung, P.; MacLaren, I.; Gregory, D. H. Rapid surfactant-free synthesis of $Mg(OH)_2$ nanoplates and pseudomorphic dehydration to MgO. *CrystEngComm* **2015**, *17* (30), 5672−5679.

(26) Cimino, S.; Lisi, L.; Romanucci, S. Catalysts for conversion of ethanol to butanol: Effect of acid-base and redox properties. *Catal. Today* **2018**, *304*, 58−63.

(27) Schroeder, E. K.; Finzel, J.; Christopher, P. Photolysis of Atomically Dispersed Rh/Al_2O_3 Catalysts: Controlling CO Coverage in Situ and Promoting Reaction Rates. *J. Phys. Chem. C* **2022**, *126* (43), 18292−18305.

(28) Fujitani, T.; Nakamura, I.; Hashiguchi, Y.; Kanazawa, S.; Takahashi, A. Effect of catalyst preparation method on ammonia decomposition reaction over Ru/MgO catalyst. *Bull. Chem. Soc. Jpn.* **2020**, *93* (10), 1186−1192.

https://doi.org/10.1021/acsomega.4c06472
ACS Omega 2024, 9, 46129−46137